# Massive and rapid predominantly volcanic $CO_2$ emission during the end-Permian mass extinction

Ying Cui[a,1], Mingsong Li[b,1], Elsbeth E. van Soelen[c], Francien Peterse[d], and Wolfram M. Kürschner[c,1]

[a]Department of Earth and Environmental Studies, Montclair State University, Montclair, NJ 07043; [b]School of Earth and Space Sciences, Peking University, Beijing 100871, China; [c]Department of Geosciences, University of Oslo, Oslo 0371, Norway; and [d]Department of Earth Sciences, Utrecht University, 3584 CB Utrecht, The Netherlands

Edited by Michael Manga, University of California, Berkeley, CA, and approved July 21, 2021 (received for review July 13, 2020)

**The end-Permian mass extinction event (~252 Mya) is associated with one of the largest global carbon cycle perturbations in the Phanerozoic and is thought to be triggered by the Siberian Traps volcanism. Sizable carbon isotope excursions (CIEs) have been found at numerous sites around the world, suggesting massive quantities of $^{13}$C-depleted $CO_2$ input into the ocean and atmosphere system. The exact magnitude and cause of the CIEs, the pace of $CO_2$ emission, and the total quantity of $CO_2$, however, remain poorly known. Here, we quantify the $CO_2$ emission in an Earth system model based on new compound-specific carbon isotope records from the Finnmark Platform and an astronomically tuned age model. By quantitatively comparing the modeled surface ocean pH and boron isotope pH proxy, a massive (~36,000 Gt C) and rapid emission (~5 Gt C yr$^{-1}$) of largely volcanic $CO_2$ source (~−15%) is necessary to drive the observed pattern of CIE, the abrupt decline in surface ocean pH, and the extreme global temperature increase. This suggests that the massive amount of greenhouse gases may have pushed the Earth system toward a critical tipping point, beyond which extreme changes in ocean pH and temperature led to irreversible mass extinction. The comparatively amplified CIE observed in higher plant leaf waxes suggests that the surface waters of the Finnmark Platform were likely out of equilibrium with the initial massive centennial-scale release of carbon from the massive Siberian Traps volcanism, supporting the rapidity of carbon injection. Our modeling work reveals that carbon emission pulses are accompanied by organic carbon burial, facilitated by widespread ocean anoxia.**

end-Permian mass extinction | compound specific carbon isotopes | $CO_2$ | Earth system model

The end-Permian mass extinction (EPME) that occurred at 251.941 ± 0.037 Mya is considered the most severe biodiversity loss in Earth history (1, 2). The EPME coincides with the eruption of the Siberian Traps, a voluminous large igneous province (LIP) that occupies 6 million square kilometers (km$^2$) in Siberia, Russia (3–5). The volcanic activity of this LIP is linked to $SO_2$ and $CO_2$ degassing generated by sill intrusion (6–10). The large amount of $CO_2$ injected into the atmosphere is thought to have led to severe global warming (11–14), catastrophic ocean anoxia (15, 16), and extreme ocean and terrestrial acidification (17–21) being lethal for life on land and in the sea (22). To date, no agreement has been reached regarding the source of the $^{13}$C-depleted carbon that triggered the global carbon cycle perturbation, the decrease in ocean pH, and the global warming across the EPME. Additionally, atmospheric $CO_2$ levels following the initial pulse of Siberian Traps volcanism and across the EPME remain poorly known (23, 24), limiting our understanding of the climate feedbacks that occur upon greenhouse gas release during this time.

To address this critical gap in our knowledge, we constrain the source, pace and total amount of $CO_2$ emissions using an Earth system model of intermediate complexity (i.e., carbon centric-Grid Enabled Integrated Earth system model [cGENIE]; *SI Appendix*) forced by new astronomically tuned $\delta^{13}C$ records from well-preserved lipid biomarkers preserved in sediments from the Finnmark Platform, Norway. The Finnmark Platform is located offshore northern Norway on the Eastern Barents Sea shelf, hosting an expanded shallow marine section (paleo-water depth roughly 50 to 100 m) where two drill cores were collected (7128/12-U-01 and 7129/10-U-01) spanning the Permian–Triassic transition (Fig. 1). A previously generated bulk organic carbon isotope record ($\delta^{13}C_{org}$) from the same core shows a two-step decline with a total carbon isotope excursion (CIE) magnitude of ~4‰ (25). Although the sedimentary organic carbon was considered primarily of terrestrial origin, small contributions from marine organic carbon production could not be excluded. Here, we use compound-specific carbon isotope analysis of both long-chain and short-chain *n*-alkanes preserved in marine sediments in the Finnmark Platform to generate separate yet directly comparable records of $\delta^{13}C$ for the terrestrial and the marine realm, respectively, across the EPME. Long-chain *n*-alkanes with a strong odd-over-even predominance (*n*-$C_{27}$ and *n*-$C_{29}$) are produced by higher plant leaf waxes, and their isotopic composition ($\delta^{13}C_{wax}$) relates to their main carbon source (i.e., atmospheric $CO_2$) (26). On the other hand, short-chain alkanes (*n*-$C_{17}$ and *n*-$C_{19}$) are derived from marine algae, and their $\delta^{13}C$ values ($\delta^{13}C_{algae}$) represent carbon in the marine realm (27, 28). To date, only a few EPME compound-specific carbon isotope studies have been reported, all of which are limited by unfavorable sedimentary facies or high thermal maturity of the organic matter (29, 30). In the present study, the exceptionally low thermal maturity of the organic matter is evident from the yellow color of pollen and spores, indicating a color index 2 out of 7 on the thermal alteration scale of Batten (31), which is equivalent to a

## Significance

**The end-Permian mass extinction event (ca. 252 Mya) is the most-severe biodiversity loss in Earth's history and is globally recognized by a rapid negative carbon isotope excursion. The trigger of this event, however, remains controversial. New paired terrestrial and marine compound-specific carbon isotope records may provide clues for this enigma. By comparing observed data to results from an isotope-enabled Earth system model, we find that a massive and rapid, predominantly volcanic $CO_2$ emission during the Siberian Traps volcanism is likely the trigger for the carbon isotope excursion and the severe mass extinction. Our findings provide quantitative constraints of how a massive and rapid increase in $CO_2$ may have influenced the marine ecosystem 252 Mya.**

Author contributions: W.M.K. designed research; Y.C., M.L., and E.E.v.S. performed research; Y.C., M.L., E.E.v.S., F.P., and W.M.K. analyzed data; and Y.C., M.L., E.E.v.S., F.P., and W.M.K. wrote the paper.

The authors declare no competing interest.

This article is a PNAS Direct Submission.



[1]To whom correspondence may be addressed. Email: w.m.kurschner@geo.uio.no, cuiy@montclair.edu, or msli@pku.edu.cn.

This article contains supporting information online at https://www.pnas.org/lookup/suppl/doi:10.1073/pnas.2014701118/-/DCSupplemental.

Published September 7, 2021.

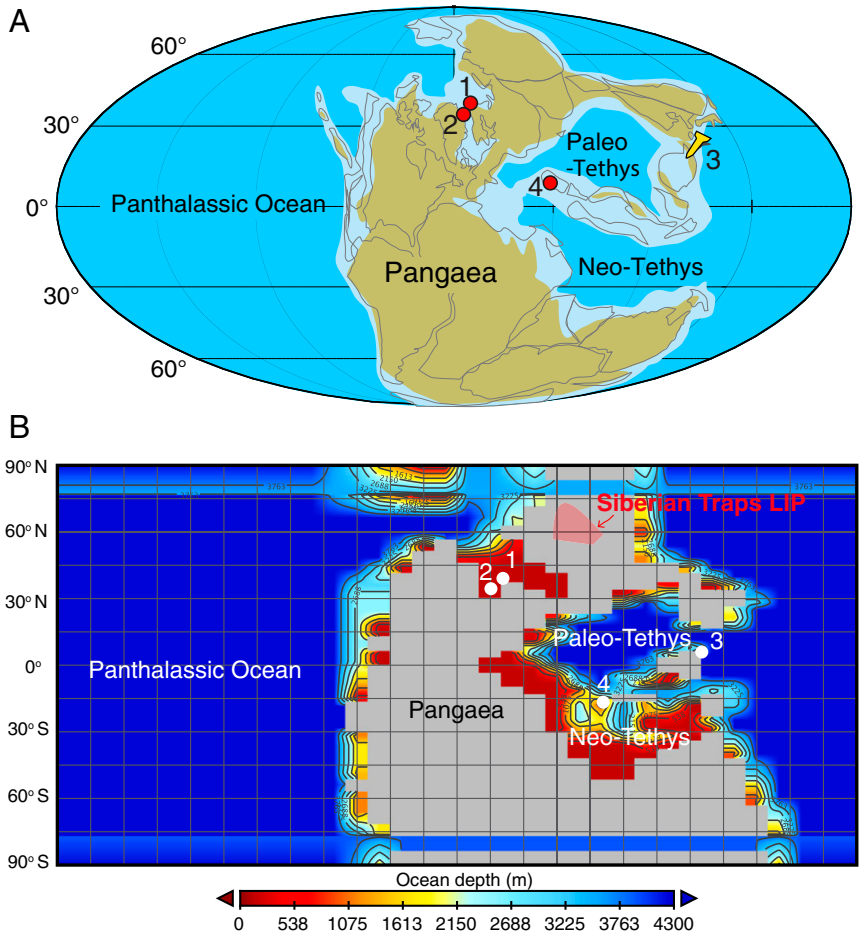


**Fig. 1.** (*A*) Paleogeographical map of the Late Permian, with former and current coastlines. Indicated are 1) the location of Finnmark cores 7128/12-U-01 and 7129/10-U-01, 2) the East Greenland site at Kap Stosch discussed in ref. 52, 3) the GSSP site for the base of the Triassic at Meishan, China, and 4) the Kuh-e-Ali Bashi site of Iran (66, 107). The map was modified after ref. 61. (*B*) Paleogeography and paleobathymetry of the Late Permian used in cGENIE.

vitrinite reflectance $R_0$ of 0.3%. Moreover, the high sedimentation rate (discussed in *Carbon Cycle Quantification Using Astrochronology and Earth System Model*) of the siliciclastic sediments at the study site allows for studying both marine and terrestrial CIE across the EPME in unprecedented detail. Taken together, the Finnmark sedimentary records enable the reconstruction of individual yet directly comparable carbon isotope records for the terrestrial and the marine realm that can be astronomically tuned and used to quantitatively assess the source, pace, and total amount of $^{13}$C-depleted carbon released during the Siberian Traps eruption that led to the EPME. Using our new compound-specific carbon isotope records, rather than marine carbonates, has several advantages: 1) new astrochronology enables a $10^4$-year temporal resolution for our paired marine and terrestrial carbon isotope records; 2) we do not need to assume a constant sedimentation rate between tie point or using diachronous biozones to compare age like those used in global compilations (24) (see Fig. 4*A*); 3) the $\delta^{13}C_{algae}$ data are not artificially smoothed as in ref. 32 to avoid underestimation of the CIE magnitude; and 4) our records are not affected by dissolution or truncation, a phenomenon common to shallow marine carbonates due to the presumed ocean acidification occurred during the EPME (18, 33). In addition, the directly comparable records of $\delta^{13}C$ for the atmosphere and the ocean offer further insights into the size of the true CIE and rate and duration of carbon emissions.

## Results and Discussion

**Fidelity of the $\delta^{13}C_{algae}$ and $\delta^{13}C_{wax}$ Records.** The long-chain *n*-alkanes in the Finnmark core show a strong odd-over-even predominance as evidenced by a carbon preference index well above 2 (Fig. 2*B* and *SI Appendix*), supporting the presumed low thermal maturity of the sediments (34). The average chain length ($ACL_{C25-C33}$) varies between 27.5 and 29.5 and shows an increasing trend upcore (Fig. 2*C*), in which higher ACL values correspond to high numbers of conifer pollen counts in the same core (e.g., at 110- to 95-m core depth), and low ACL values are associated with the pteridosperm (seed fern)-dominated ecosystem that existed prior to the EPME (Fig. 2*A*). The interval with intermediate ACL (116- to 108-m core depth) is linked to a spore peak and the first negative excursion in the $\delta^{13}C$ record of sedimentary organic matter ($\delta^{13}C_{org}$) (Fig. 2*F*), suggesting that local terrestrial ecosystem reorganization may have modified the original $\delta^{13}C_{org}$ signal across the EPME at this site (25, 35). Short-chain *n*-alkane abundances show more variation throughout the section and are sometimes dominant over the longer chain *n*-alkanes, indicative of changing marine and terrestrial contributions to the total carbon pool (Fig. 2*D*).

In addition to $\delta^{13}C_{org}$ (Fig. 2*F*), we report the $\delta^{13}C_{algae}$ as the weighted-average of *n*-$C_{17}$ and *n*-$C_{19}$ alkane $\delta^{13}C$ values and $\delta^{13}C_{wax}$ as the weighted-average of *n*-$C_{27}$ and *n*-$C_{29}$ alkane $\delta^{13}C$ values (Fig. 2*G*). The $\delta^{13}C_{algae}$ record displays a two-step negative CIE, of which the first exhibits a magnitude of ~5‰ and the

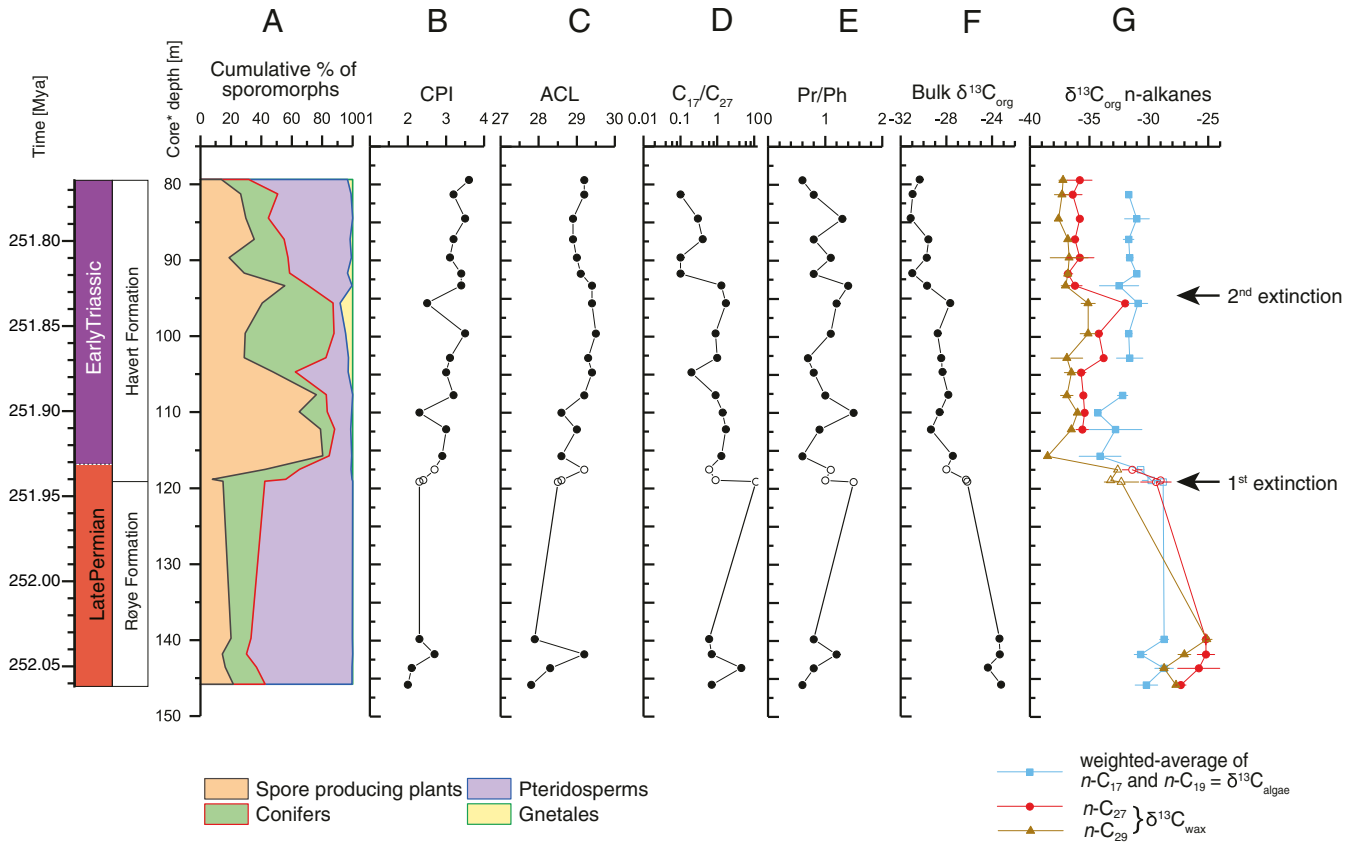


**Fig. 2.** (*A*) Relative abundances of major groups of terrestrial palynomorphs. (*B*) Carbon preference index. (*C*) ACL of *n*-alkanes $C_{25}$-$C_{33}$. (*D*) Ratio between $C_{17}$ and $C_{27}$ *n*-alkane abundance. (*E*) Pristane/phytane (Pr/Ph) ratio. (*F*) Bulk organic $\delta^{13}C$ values ($\delta^{13}C_{org}$) measured in this study. (*G*) Compound-specific $\delta^{13}C$ values of $C_{27}$ and $C_{29}$ *n*-alkanes ($\delta^{13}C_{wax}$) and the weighted average of $C_{17}$ and $C_{19}$ *n*-alkanes ($\delta^{13}C_{algae}$). Error bars represent the SD based on multiple analysis of the same sample. Individual values and SDs are given in *SI Appendix*, Table S6, and core depth refers to core 7128/12-U-01 (indicated by solid marks) with samples from 7129/10-U-01 (indicated by hollow marks) correlated as shown in *SI Appendix*, Fig. S2 and Table S5. The astronomically tuned age model (left) is detailed in Fig. 3.

second a magnitude of ~1.5‰ (Fig. 2*G*), similar to the record of $\delta^{13}C_{org}$ (~5‰ and ~2‰ during the two negative CIEs, respectively) (Fig. 2*F*). The $\delta^{13}C_{wax}$ shows a similar trend to the $\delta^{13}C_{algae}$ record during the two negative CIEs (Fig. 2*G*), although the magnitude is twice that in $\delta^{13}C_{algae}$. Such terrestrial CIE amplification is also seen from several other Permian-Triassic boundary (PTB) sites in China (24, 36), Australia, and Antarctica (37). The amplified CIE magnitude in $\delta^{13}C_{wax}$ may be partly attributed to rising atmospheric $CO_2$ levels (38) and augmented by changes in terrestrial vegetation types and hydrological cycle (39). However, a plausible alternative interpretation of the amplified terrestrial CIE signal is that the surface waters of the Finnmark platform were out of equilibrium with the rapid release of carbon from the massive volcanism. The astronomically tuned age model (see *Materials and Methods*) allows for detailed correlation of the two negative CIEs in the biomarkers: the first CIE is associated with the EPME between 251.941 ± 0.037 Mya and 251.880 ± 0.031 Mya (1), and the second CIE appears to immediately predate the second extinction pulse at 251.761 ± 0.06 Mya (40) (see Fig. 5 and in *SI Appendix*). The onset of the first CIE in $\delta^{13}C_{algae}$ occurs at 119.1-m core depth (Fig. 2, 251.941 Mya or time 0 in our model simulation) (1), and the $\delta^{13}C_{algae}$ rapidly declines to −34.1‰ at 115.7 m (251.926 Mya) followed by a small rebound to −32.8‰ at 112.2 m (251.910 Mya) before reaching a minimum value of −34.3‰ at 110.0 m (251.900 Mya). If we define the CIE onset as the most rapid decline in $\delta^{13}C_{algae}$, then the CIE onset duration is calculated to be 15 Kyr (from 251.941 to 251.926 Mya). The $\delta^{13}C_{algae}$ remain >2‰ lower than the pre-CIE values, while both $\delta^{13}C_{org}$ and $\delta^{13}C_{wax}$ stay >6‰ lower than their pre-CIE values, suggesting changes in terrestrial vegetation types and hydrological cycle persisted in the terrestrial realm regionally.

The $\delta^{13}C_{algae}$ record is considered representative of the ocean dissolved inorganic carbon (DIC) system across the EPME for several reasons. Two factors that may have affected the marine $\delta^{13}C_{algae}$ record, marine anoxia, and changes in microbial communities (e.g., ref. 41) do not play a role on the Finnmark Platform. Firstly, the widespread interval of anoxic conditions that developed in many locations that may have decreased the $\delta^{13}C_{org}$ values (25, 42) during the EPME (15, 43–48) is not observed in the Finnmark cores because of low-density bioturbation (49, 50) and the absence of amorphous organic matter (50, 51). This is in agreement with pristane/phytane (Pr/Ph) ratios being greater than 1 for most of the samples (Fig. 2*E*). Only short intervals with dysoxic conditions have been identified (50), which correlate with Pr/Ph ratios of 0.6 at 116 m, 103 m, and 90 m. However, the $\delta^{13}C_{org}$ and $\delta^{13}C_{algae}$ records do not show a consistent correlation with the temporary dysoxic conditions indicated by low Pr/Ph values (*SI Appendix*). Because of this rather-stable marine depositional environment, we presume that the composition of the marine microbial community remained unchanged. This is a plausible scenario as hopane/sterane ratios over the Permian–Triassic boundary interval at Kap Stosch on East Greenland (Fig. 1, location 2) are fairly stable around 1.5 to 2 in a similar depositional setting (52). Similar to terrestrial higher plants, carbon isotope fractionation of marine algae can also be sensitive to changes in atmospheric $CO_2$ (53, 54). The increased $CO_2$ may have amplified the Finnmark algae

biomarker, but the ocean biogeochemistry may have muted such effect and exerts little net change to its overall CIE signal (Fig. 2*F*). Nevertheless, the magnitude of the CIE for $\delta^{13}C_{algae}$ remains similar to the range of 4 to 5‰ reported from the Paleo-Tethys marine carbonate (55) (Fig. 3). In order to better understand the effects of large-scale $CO_2$ release on climate and environmental conditions and thus identifying the exact cause of the extinction, it is crucial to constrain the magnitude of the excursion to estimate the rate and magnitude of $CO_2$ release (23, 32, 56). Many published Late Permian $\delta^{13}C$ records for the marine realm are based on bulk carbonates ($\delta^{13}C_{carb}$), most of which are from carbonate platforms in the Paleo-Tethys Ocean (55). One potential bias in the marine carbonate records is the sediment mixing that can have an effect on the $\delta^{13}C_{carb}$, as shown for deep-sea sections during the Paleocene-Eocene Thermal Maximum (PETM) (57). Additionally, some of these carbonates may be highly condensed due to extremely low accumulation rates (2, 58), which makes it difficult to distinguish the EPME from the Permian–Triassic boundary (1, 59). For example, the Meishan Global Boundary Stratotype Section and Point (GSSP) section in South China (Fig. 1, location 3) is impacted by extremely low sedimentation rate (<1 cm $Kyr^{-1}$), but the magnitude of CIE (~4 to 5‰) is similar to that in $\delta^{13}C_{algae}$ from this study. On the other hand, one of the most expanded carbonate sections, the Kuh-e-Ali Bashi section in Iran (Fig. 1, location 4 and Fig. 3*F*), shows several negative isotope excursions in $\delta^{13}C_{carb}$ record of the Late Permian and Early Triassic (60), during which the magnitude of the CIE associated with the EPME is about 4‰, similar to the CIE magnitude observed in the $\delta^{13}C_{algae}$ record reported here (Fig. 3), another line of evidence supporting that $\delta^{13}C_{algae}$ is representative of the ocean DIC. In contrast, both $\delta^{13}C_{wax}$ data and $\delta^{13}C_{plant}$ data from cuticles and wood of $C_3$ land plant remains in South China (24) show augmentation in their CIE magnitude compared to $\delta^{13}C_{algae}$ and $\delta^{13}C_{carb}$ (Fig. 4 *A* and *B*). Therefore, we suggest that the *n*-alkanes in the Finnmark section are faithful recorders of the global surface ocean carbon cycle perturbation resulting from their pristine preservation. Although our sampling resolution is lower than that of existing bulk marine carbonate records, our new compound-specific carbon isotope records are the highest of their kind for this time interval and enable us to separate terrestrial and marine signals (Fig. 4 *A* and *B*). In addition, our records are more suitable for the isotope inversion modeling because the astrochronology allows for the age of each sample to be very well constrained. In contrast, despite the high temporal resolution for marine bulk carbonate records, the age of these samples is only interpolated from lithostratigraphy or biostratigraphy, which makes the high sampling resolution less relevant. Additionally, the high sedimentation rates of the siliciclastic sediments at the Finnmark Platform provide us with the high-quality records required to establish high-fidelity geochronology based on cyclostratigraphy (61).

**Carbon Cycle Quantification Using Astrochronology and Earth System Model.** To quantify the carbon cycle perturbations across the EPME, we constructed a high-resolution astrochronological age model for the Finnmark core. Time series analysis of the total gamma ray intensity at core 7128/12-U-01 provides a floating astronomical time scale for the carbon isotope records (*SI Appendix*, *Materials and Methods*). The power spectrum of the gamma ray series shows that the dominant cycles are at 23 m, 7.4 m, 5.5 m, 4 m, and 2.7 m (*SI Appendix*, Figs. S6–S8). The evolutionary power spectrum indicates that the 23-m cycles represent the dominating cyclicity throughout the series and that the 5- to 7-m cycles are the leading cyclicities across the Permian–Triassic boundary interval (ca. 125- to 105-m core depth; *SI Appendix*, Fig. S9). Correlation Coefficient and time scale optimization analyses suggest that the optimal mean sedimentation rate is ~22.4 cm/Kyr (*SI Appendix*, Figs. S10 and S11), which enables generating a 432-Kyr-long floating astrochronology for the Finnmark core (Fig. 3). The initial CIE is correlated with the EPME onset from the GSSP at Meishan, South China (1) (*SI Appendix*, Figs. S13 and S14) and is set to a 251.941 ± 0.037 Mya age (Meishan) (1) for the construction of an absolute astronomical time scale. The Finnmark Platform CIE duration (115.7- to 93.3-m core depth) encompasses approximately one eccentricity cycle (Fig. 3*A*), which is comparable to the Meishan GSSP for the basal Triassic (*SI Appendix*, Fig. S14). Cyclostratigraphy of the Meishan uranium series suggests that the two pulses of extinction lasted for about 40 Kyr, and the largest CIE lasted for about 6 Kyr (61). Other estimations of the EPME interval at Meishan are 60 ± 48 Kyr based on uranium–lead (U-Pb) dating (1) and 83 Kyr based on cyclostratigraphy (62). However, the highly condensed nature of the Meishan section limits the confidence of its astrochronology. Here, the high sedimentation rate (22.4 cm/Kyr versus <1 cm/Kyr at Meishan and Daxiakou of South China) (61) associated with continuous deposition provides a more reliable estimation of the CIE duration of 109 Kyr and a CIE onset duration of 15 Kyr. This slightly longer duration of the end-Permian CIE compared to previous estimates implies that the carbon cycle within the ocean and atmosphere system has a longer time to respond and recover from perturbation. The end-Permian CIE began at the peak of a 100-kyr cycle at both the Finnmark Platform and the GSSP Meishan sections (*SI Appendix*, Fig. S14), providing additional evidence for the global correlation of the carbon isotope records.

Previous modeling work inverted the $\delta^{13}C$ record of marine carbonate from the GSSP Meishan section (32, 63), which is impacted by the highly condensed nature of the site (2). Inverting $\delta^{13}C$ alone also suffers from nonunique solutions when determining the carbon emission flux by assuming the isotopic composition of an unknown source (32, 63). We improved upon previous work by using the surface ocean pH records (17, 20) and sea surface temperature records (14, 64–66) as additional constraints to determine the most-plausible carbon source and associated carbon emission rate by minimizing the root mean square root (RMSE) (*SI Appendix*). This approach allows for the determination of the best-matched $\delta^{13}C$ value of the $CO_2$ emitted and therefore quantifying the paleoclimatological effects of this important greenhouse gas. Using the newly constructed astrochronology in the Finnmark Platform, the pace of $CO_2$ changes across the EPME is estimated via carbon isotope inversion based on $\delta^{13}C_{algae}$ along with the age model described above using cGENIE model and further constrained by $\delta^{11}B$ as a proxy of pH (17) and $\delta^{18}O$ as a proxy of temperature. The initial and boundary conditions of the end-Permian are adapted from ref. 32, except that the initial $pCO_2$ is set to be 440 ppmv following recent studies by Li et al. (67) using the stomatal ratio and Wu et al. (24) using the $\delta^{13}C$ of fossil $C_3$ plant remains. We ran simulations that consider a broad combination of model parameters and assumptions associated with proxy interpretation (*SI Appendix*, Tables S1 and S2). Our model ensemble includes seven simulations (*SI Appendix*, Table S3), each associated with a unique isotopic signature of the carbon source forced by the compound-specific carbon isotope records of marine algae and the astrochronology generated in this study (Figs. 3 and 4). Based on the smallest RMSE between our modeled pH and the proxy records, we identify that the best-matched scenario is associated with $\delta^{13}C = -15‰$ (refer to *SI Appendix* for the RMSE results). This best-fit scenario is associated with a large pulse of mainly volcanic $CO_2$ from the Siberian Traps volcanism (53% if we assume the $\delta^{13}C$ of peridotite-derived $CO_2$ is −6‰ as in ref. 68 and 77% if the $\delta^{13}C$ of recycled crust $CO_2$ is −12‰ as in ref. 69), if the remaining $CO_2$ is derived from sedimentary organic matter oxidation (9) or coal combustion (70). This scenario is associated with a massive amount of total $CO_2$ emission (approaches ~36,000 Gt C) over the 168 Kyr simulation duration and a maximum emission rate of 4.5 Gt C $yr^{-1}$ (Fig. 5), roughly half the size of current carbon emission rate (71, 72). The atmospheric

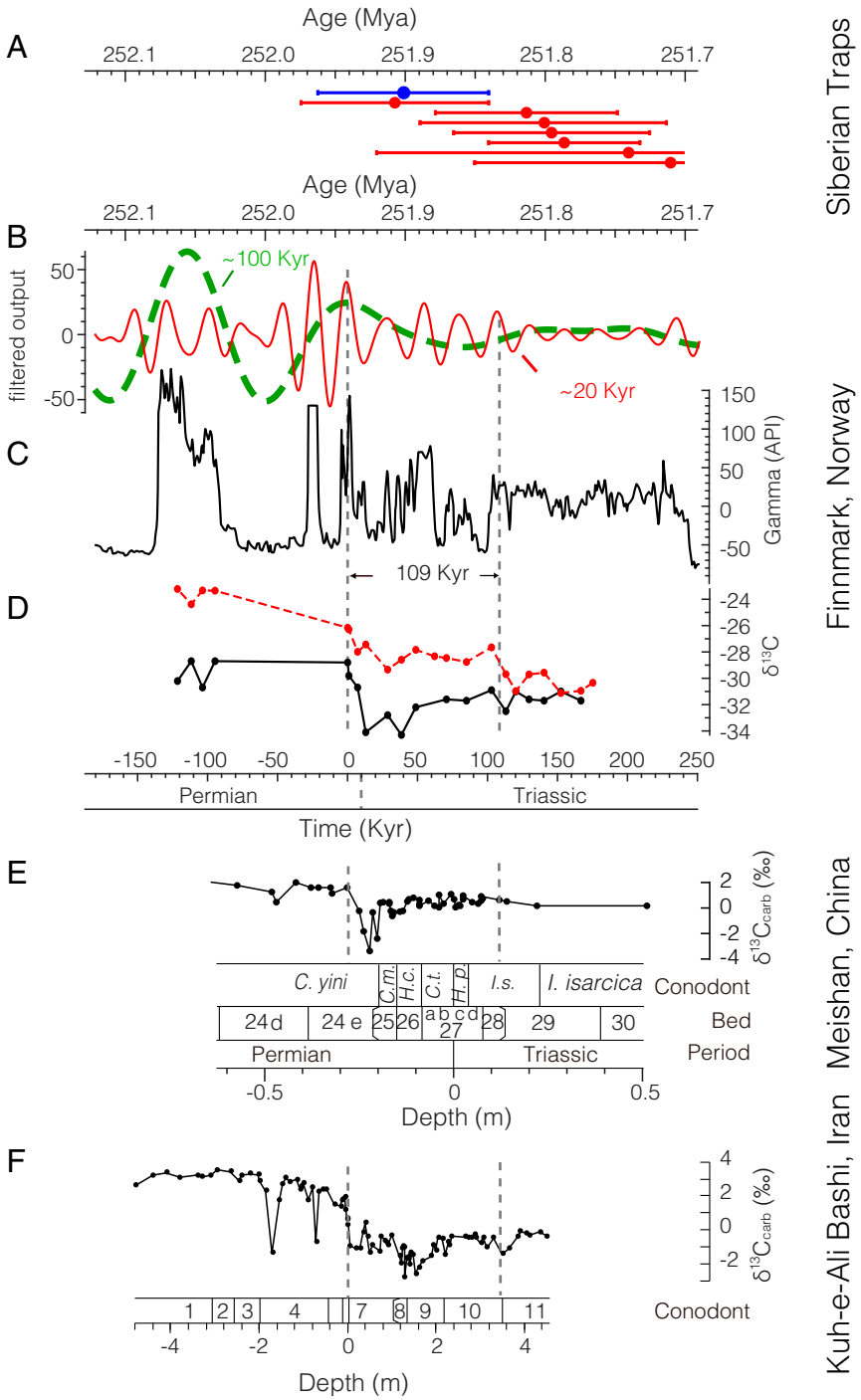


**Fig. 3.** Time series analysis. (*A*) Weighted mean uranium-lead (U-Pb) dates reported with 2σ analytical uncertainties for Siberian Traps LIP sills (red) and pyroclastic rocks (blue) (5). (*B*) ~100-Kyr eccentricity (dashed green) and 20-Kyr precession (red) Gauss bandpass-filtered cycles (passband is 0.0085 ± 0.0025 and 0.045 ± 0.01 cycles/Kyr, respectively). (*C*) Time-calibrated gamma ray series in American Petroleum Institute (API) unit from cores 7128/12-U-01. (*D*) Time-calibrated $\delta^{13}C_{org}$ (red) and $\delta^{13}C_{algae}$ (black) across the Permian–Triassic transition. (*E*) $\delta^{13}C_{carb}$ record for the Meishan section, China (2) shown with bed numbers and conodont zones (108). Conodont zones: *C. m.*=*Clarkina meishanensis*, *H. c.* = *Hindeodus changxingensis*, *C. t.* = *C. taylorae*, *H. p.* = *H. parvus*, and *I.s.* = *Isarcicella staeschei*. (F) $\delta^{13}C$ data at Kuh-e-Ali Bashi section of Iran (66, 107) shown with conodont zones (109, 110): 1) *C. changxingensis*, 2) *C. bachmanni*, 3) *C. nodosa*, 4) *C. yini*, 5) *C. abadehensis*, 6) *C. hauschkei*, 7) *H. praeparvus-H. changxingensis*, 8) *M. ultima-S. ?mostleri*, 9) *H. parvus*, 10) *H. lobota*, and 11) *I. staeschei*.

$pCO_2$ increases from ~440 (67) to ~7,390 ppm when $\delta^{13}C_{algae}$ reaches its first minimum, with the maximum $pCO_2$ value falling in the upper range of a recent $CO_2$ reconstruction using an independent estimate based on carbon isotopes of fossil $C_3$ land plant remains across the EPME (24). This 13× increase in atmospheric $CO_2$ causes global temperature to rise from 25 to 40 °C, in accordance with temperature proxy data based on well-preserved brachiopod shells (13, 14) but slightly smaller than the temperature proxy data using conodonts (64–66), suggesting that the $\delta^{13}C_{source}$ may have become higher than −15‰ during the warmest interval,

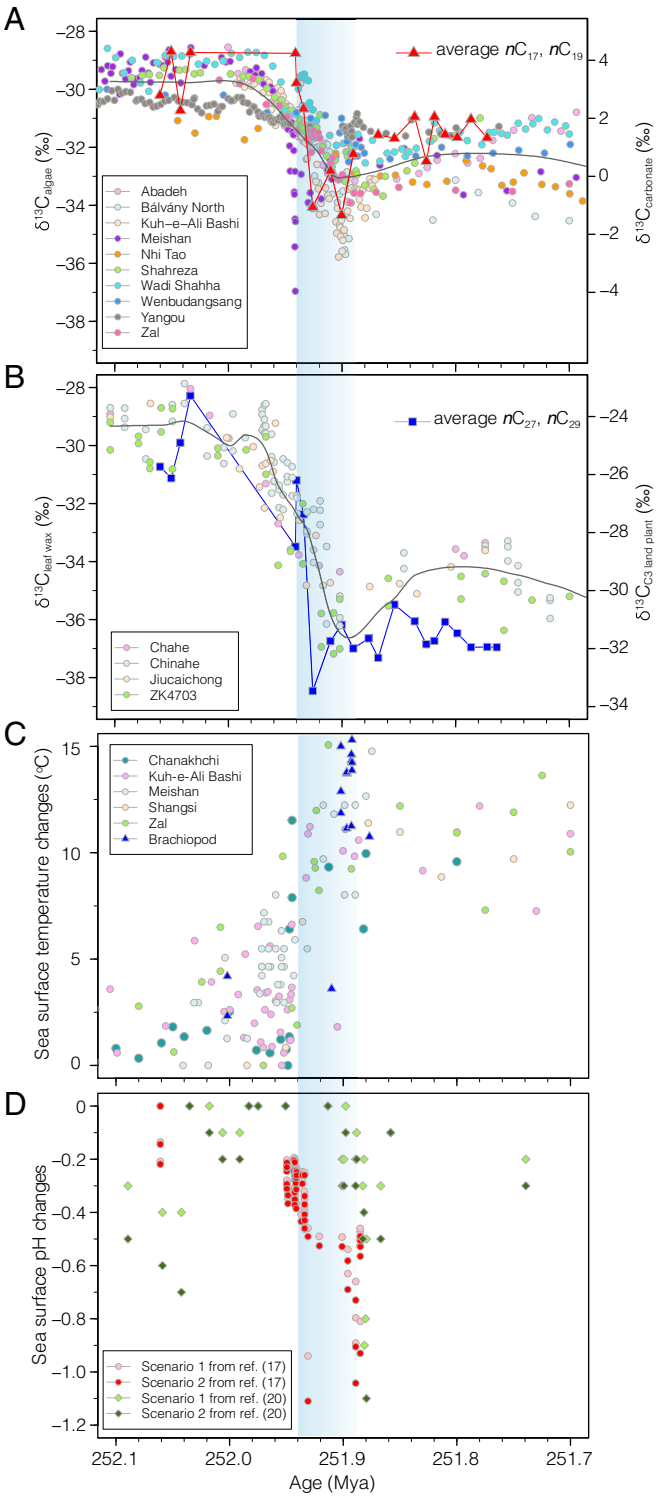


**Fig. 4.** Synthesized proxy records of carbon isotopes from marine carbonates and fossil $C_3$ land plants remains, sea surface temperature, and pH. (*A*) Comparison between $\delta^{13}C_{algae}$ and global marine carbonate carbon isotopes from sites at Abadeh, Kuh-e-Ali Bashi, Shahreza, and Zal in Iran, Meishan, Wenbudangsang, and Yanggou in South China, at Bálvány North in Hungary, and at Nhi Tao in Vietnam (24). (*B*) Comparison between $\delta^{13}C_{leaf}$ wax and the $\delta^{13}C$ of sedimentary leaf cuticles and wood of $C_3$ land plants from South China (24). (*C*) Reconstructed sea surface temperature data using conodont fossils (circles) (24) and brachiopods (triangles) (14). The conodont-based temperature data are from sites in the Paleo-Tethys, including Chanakhchi, Kuh-e Ali Bashi, Meishan, Shangsi, and Zal. (*D*) Relative changes in sea surface pH based on boron isotope proxy from ref. 17 and ref. 20. Pink and red circles are data from scenario 1 and scenario 2 in ref. 17, and green and blue diamonds are data from scenario 1 and scenario 2 in ref. 20.

consistent with varying $\delta^{13}C_{source}$ with evolving degassing style. The $CO_2$-driven warming response of the global ocean likely differ due to changes in the ocean circulation pattern. Our model results show extreme warmth in the eastern Paleo-Tethys relative to in the western Paleo-Tethys (*SI Appendix*, Fig. S25), providing spatial variability that can be further compared with temperature proxy data for the eastern and western Paleo-Tethys (11), a feature that cannot be revealed in the one-dimensional biogeochemical box model used in (17). Intriguingly, our preferred $\delta^{13}C_{source}$ of −15‰ coincides with an independent estimate based on a calcium isotopic mass balance model (19) and lies within the range (−11 to −17‰) suggested by Gutjahr et al. (73) for the PETM, indicating the two events share similar trigger mechanisms. Indeed, the PETM has been linked to the North Atlantic Igneous Province with a volume as large as 150,000 $km^3$ (74). It is important to note that the PETM is only associated with a small extinction of the benthic foraminifera due to the presumed slow rate of carbon emission (75, 76). In the following, we compare the carbon emission history of the EPME based on our inverse modeling and results from the literature.

The simulated $CO_2$ emission exhibits at least two pulses that appear to be global (pulse 1 and 2) (*SI Appendix*). Prior to the main emission pulse, a small amount of carbon was emitted at a peak rate of 2.7 Gt C $yr^{-1}$ (average rate 1.6 Gt C $yr^{-1}$) that lasted for 1.9 Kyr (maintaining emission rate at > 1 Gt C $yr^{-1}$), which reflects a near-instantaneous drop in $\delta^{13}C_{algae}$ during the CIE onset. This initial emission pulse is not seen in the previous modeling work (17, 32) (Fig. 5*C*) and therefore may be an artifact from local effects. The two major $CO_2$ emission pulses (labeled pulse 1 and pulse 2) are associated with a maximum carbon emission rate of 4.5 Gt C $yr^{-1}$ and 1.9 Gt C $yr^{-1}$ (average 2.6 Gt C $yr^{-1}$ and 1.5 Gt C $yr^{-1}$) and lasted for 8.3 Kyr and 9.1 Kyr respectively (maintaining emission rate at > 1 Gt C $yr^{-1}$). The largest emission pulse (pulse 1) is two times larger than the estimate from a previous model inversion (32) using the GSSP Meishan carbon isotope record (Fig. 5*A*) and 7× as large as the estimate in ref. 17 (0.7 Gt C $yr^{-1}$) based on a forward biogeochemical model. This discrepancy likely resulted from the smaller magnitude of the CIE recorded in shallow marine carbonate sections, the lack of astrochronology, and a lower assumed $\delta^{13}C_{source}$ in these previous studies (17, 32). The model results from slower emission rate and lower $pCO_2$ (~4,400 ppm) in Jurikova et al. (17) did not capture the full magnitude of the proxy estimate of pH decline and temperature rise (their Fig. 2 *C* and *H*) and therefore higher emission rate and $pCO_2$ are required to better match the proxy data. The two main pulses appear to overlap in timing with the intrusive phase of the Siberian Traps volcanism (4, 8, 9) (Fig. 5 and *SI Appendix*, Table S5) following the onset of sill complex and magmatic intrusion (251.907 ± 0.067 Mya) (4), which supports a direct link between the Siberian Traps volcanism and the $CO_2$ emission (Fig. 5). The degree of warming (>10 °C) and acidification (ΔpH ~1), the CIE magnitude (~5‰), and the CIE onset duration (15 Kyr) dictate that the carbon emission rate during the peak EPME is up to 7× faster than that during the PETM (0.6 Gt C $yr^{-1}$ in ref. 73 and 1.7 Gt C $yr^{-1}$ in ref. 75). The final carbon emission pulse lasted longer (10.3 Kyr) but has a much smaller peak emission rate of 1.0 Gt C $yr^{-1}$ (average 0.8 Gt C $yr^{-1}$), although it is not seen in previous work and may be a local signal (Fig. 5*C*). In addition to the rapidity of the carbon injection during the peak EPME, the cumulative carbon emission (36,200 Gt C) amounts to 3× that across the PETM (10,200 to 12,200 Gt C) (Fig. 5*D*) and may have been the ultimate driver of the much-more-severe ecological consequences at the end of the Permian Period. The ~36,000 Gt C cumulative carbon added

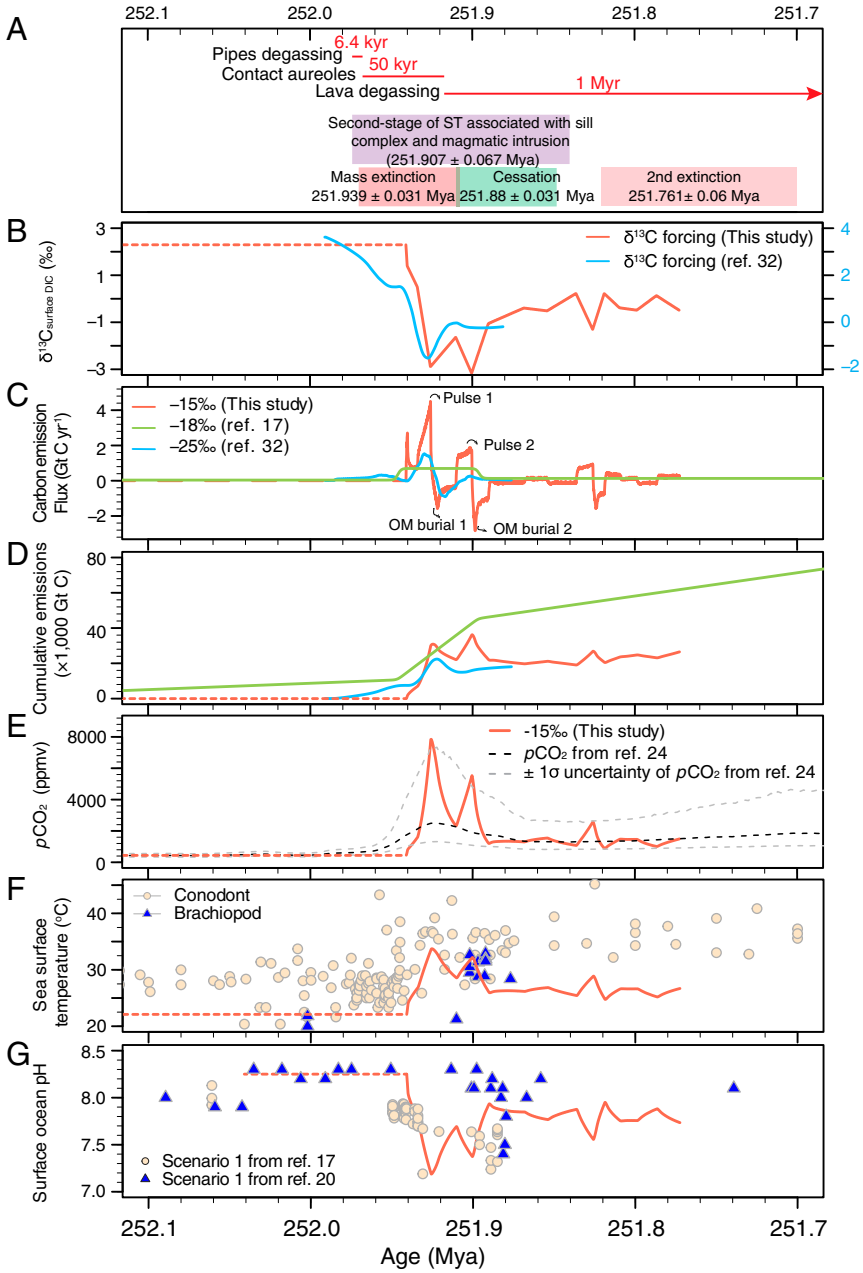


**Fig. 5.** Key model results from the RMSE-determined best fit. (*A*) Links between the EPME and the timing of Siberian Traps volcanism. Age of mass extinction is 251.939 ± 0.031 Ma based on Shen et al. (106) and age of second-stage of Siberian Traps volcanism is 251.907 ± 0.067 Ma from Burgess et al. (4) Duration of pipe degassing, contact aureoles, and lava degassing are from Svensen et al. (9), assuming that the onset age is 251.907 ± 0.067 Ma. Also shown is the age of the extinction cessation at 251.88 ± 0.031 Ma based on Meishan Bed 28 (5) and the age of second extinction in the earliest Triassic at 251.761 ± 0.06 Ma (40). Note that the red curve is based on $\delta^{13}C_{algae}$ assuming a constant fractionation between algae and DIC of 31‰, which is within the range of maximum fractionation for marine algae (111–113). (*B*) $\delta^{13}C$ forcing comparison of the surface DIC for this study and (32) derived from the GSSP Meishan section after loess curve fitting. (*C*) Modeled carbon emission rate in Gt C $yr^{-1}$ from the best-fit scenario (red) and comparison to the carbon emission rate for the organic matter scenario in (32) (blue) and Jurikova et al. (17) (green). (*D*) Modeled cumulative carbon emission in Gt C from the best-fit scenario (red) and comparison to the carbon emission rate for the organic matter scenario in Cui et al. (32) (blue) and Jurikova et al. (17) (green). (*E*) Modeled changes in atmospheric $pCO_2$ in ppmv from the best-fit scenario (red) and the reconstructed continuous $pCO_2$ from Wu et al. (24) based on carbon isotopes of fossil $C_3$ plant remains. (*F*) Modeled changes in global sea surface temperature in °C from the best-fit scenario (red) and comparison to reconstructed Paleo-Tethys ocean temperature based on $\delta^{18}O$ of well-preserved conodonts (beige circles) (24) and brachiopods (blue triangles) (14). (*G*) Modeled surface ocean pH decline from the best-fit scenario (red) and comparison to the boron isotope proxy pH reconstruction from Jurikova et al. (17) and Clarkson et al. (20). Dashed red lines in *B*–*G* represents the steady-state condition from the 200-Kyr-long spin-ups.

in the first 15,000 y of our simulation is well within the range of estimated total emission from phreatomagmatic pipe degassing, contact aureoles, and lava degassing from the Siberian Traps volcanism (9, 74, 77) (*SI Appendix*) and similar to an estimate from ref. 17, although these authors allow the mantle-dominated carbon emission to continue following the CIE. Nevertheless, we find that there is large uncertainty associated with the total degassing budget from the Siberian Traps volcanism and that the

$\delta^{13}C_{source}$ values could deviate from −15‰ depending on the eruption style. Indeed, the $\delta^{13}C_{source}$ value may become higher through the emission period, with more mantle carbon later on during Siberian Traps emplacement. More mantle carbon would have led to higher $pCO_2$ modeled here and could explain the low pH values observed following "pulse 2" in Fig. 5. Besides the emission from the degassing from the Siberian Traps, rapid degradation of labile organic carbon from rapidly accumulating organic matter in the ocean (78) and from catastrophic terrestrial soil erosion (79) may have augmented the carbon emission flux. Each carbon emission pulse is followed by negative fluxes necessary to explain the carbon isotope recovery (maximum carbon sequestration following pulse 2, at −2.8 Gt C $yr^{-1}$), which indicate organic carbon burial in the ocean (Fig. 5). Increased organic carbon burial is facilitated by the widespread ocean anoxia (15, 16, 80) and high phosphate concentration resulting from increased continental weathering that promoted primary productivity in the surface ocean (81, 82).

Similar to nutrient levels, the alkalinity of the ocean is expected to increase due to increased silicate weathering rate after a large pulse of $CO_2$ emission (83). Freshly erupted basalt from the Siberian Traps volcanism may have accelerated the $CO_2$ consumption. However, the eruption emplaced volcanic rocks into areas on the Earth's surface where weathering rates are relatively low, and the expected continental weathering increase would be acting on preexisting transport-limited areas of the Earth's surface (84–89). This limited effect of $CO_2$ drawdown may have led to a failure of the silicate weathering and extended the warming well into the Early Triassic (90). As an important caveat, the model does not consider explicitly expressed lithology, despite the inclusion of a temperature-dependent silicate weathering feedback. We note a 2.7× increase in the weathering flux (30 Tmol $yr^{-1}$ to 79 Tmol $yr^{-1}$) from the elevated $CO_2$ and temperature (*SI Appendix*), but the increased weathering flux did not drive a full recovery in $pCO_2$ and temperature, suggesting the temperature-dependent silicate weathering feedback alone is insufficient to recover the climate system within the model simulation duration. The increased weathering flux led to higher alkalinity in the surface ocean, which increases from 4.5 to 5.3 mmol $kg^{-1}$ when the maximum alkalinity is reached at 41 Kyr from the CIE onset. The surface ocean pH declined by 1.1 unit from 8.3 to 7.2, which is consistent with the amount of pH decline based on boron isotope proxy from well-preserved brachiopods in the Southern Alps of northern Italy (17) (0.9 to 1.1 unit decline for the two scenarios associated with whether vital effects affect the $\delta^{11}B$-pH dependency) and selected micrite and early cemented grainstones from the Musandam Peninsula in United Arab Emirates (20) (0.9 to 1.1 unit decline assuming −34 and −36.8‰ $\delta^{11}B_{seawater}$ value). It should be noted that these pH change estimates are likely conservative if ancient calcifying brachiopods have larger vital effects than assumed in these studies. Higher $pCO_2$ also resulted in lower benthic oxygen levels, which reduced significantly from 152 μmol $kg^{-1}$ to 0 μmol $kg^{-1}$ at ∼9.9 Kyr from the CIE onset. The cumulative carbon emission reached ∼30,800 Gt C following emission pulse 1, which corresponds to maximum $pCO_2$ (7,844 ppmv) and coincides with the maximum modeled temperature (33.7 °C), similar to the proxy record based on oxygen isotope from well-preserved brachiopod shells (33 °C; Fig. 5 *B*–*D*). Emission pulse 2 was followed by a second peak of $pCO_2$ (5,530 ppmv) and temperature (32.2 °C). The lowest pH also coincides with the emission pulse 1, underwriting the importance of a rapid $CO_2$ emission associated with the Siberian Traps volcanism. This model inversion strongly supports that it is the rapid and massive $CO_2$ that led to the abrupt decline in pH, extreme increase in surface ocean temperature, and the combined environmental effects that drove the mass extinction at 251.939 ± 0.031 Mya. The transition from mainly flood lavas to predominantly sill intrusions during the Siberian Traps volcanism (4) coincide with the onset of the global CIE and the EPME, providing a valid trigger mechanism for the $CO_2$ release from volcanic $CO_2$. Elevated mercury levels across the EPME in sections found in many locations, including China (91, 92), Arctic Canada (93, 94), and the United States (95), are supportive of the volatile gas emissions during sill intrusion and lava degassing. Recent mercury mass balance modeling provides additional quantitative constraints to the mercury loading related to volcanic eruption and sill intrusion (96, 97). The largely volcanic $CO_2$ scenario presented here, if correct, can provide fundamental implications to understand the Earth system response to the large pulse of $CO_2$ emission and the relationship between rapid climate change and mass extinction through time.

In addition to the paleoclimate implications from the modeling study on carbon emission, we can gain further insight on the controls of the CIE amplification in $\delta^{13}C_{wax}$. This amplification could be attributed to three factors: 1) an increase in atmospheric $CO_2$ levels (38); 2) changes in hydrological conditions and vegetations (39); and 3) a disequilibrium between the surface ocean and the atmosphere (98). The amount of amplification due to increased $pCO_2$ is highly dependent on the initial $pCO_2$ prior to the EPME (i.e., a lower initial $pCO_2$ will yield a larger photosynthetic fractionation and vice versa). The ∼440-ppm $CO_2$ level reconstructed from stomatal proxies (67) may underestimate the $pCO_2$ in the latest Permian (23), which could lead to an overestimation of the increase in photosynthetic fractionation. If the initial atmospheric $pCO_2$ was higher than that indicated by stomatal proxies (i.e., ∼2,800 ppm as in ref. 32), the increase in photosynthetic discrimination due to increased $pCO_2$ is only ∼1‰ (*SI Appendix*), which allows for an alternative interpretation for the amplified terrestrial CIE. Terrestrial plant leaf waxes directly sample the atmosphere reservoir, which suggests that the atmosphere changed much more than what is observed in the equilibrium ocean response, implying that the change may have occurred faster than the equilibration time between these reservoirs during the EPME. A larger atmospheric CIE than that in the surface waters is observed for a very-rapid carbon release scenario for the PETM in Kirtland Turner and Ridgwell (99) in cGENIE. Such an alternate possibility suggests that the surface waters of the Finnmark platform were out of equilibrium with the initial massive centennial-scale release of carbon as a result of the massive Siberian Traps volcanism. A significantly larger atmospheric CIE magnitude during the PTB implies the carbon emission is rapid and massive, which is consistent with our modeling results. A critical rate of the Earth's carbon cycle perturbation may have been reached, which triggered magnifying feedbacks and ultimately drove the Earth's system beyond a threshold and lead to the mass extinction (100, 101).

## Conclusions

Late Permian shales and siltstones from the Finnmark Platform are ideal for compound-specific isotope analyses and the subsequent carbon cycle quantification, as the organic matter is well preserved and marine environmental conditions remained stable. The resulting compound-specific carbon isotope records reveal a first, simultaneous negative shift in $\delta^{13}C_{algae}$ and $\delta^{13}C_{wax}$ of 4 to 5‰ and 10 to 11‰, respectively. This first negative CIE in the Finnmark $\delta^{13}C$ records is linked to the globally recognized negative shift that marks the EPME, while the second negative CIE immediately predates the second small-scale extinction in the earliest Triassic (Fig. 5). The high sedimentation rate associated with continuous deposition in the Finnmark core enables a more reliable astrochronological estimation of the CIE onset duration of 15 Kyr and a total CIE duration of 109 Kyr. The high-resolution $\delta^{13}C_{algae}$ record presented in this study is similar in shape to the global CIE seen elsewhere (Fig. 4 *A* and *B*) in that they show similar CIE magnitude and exhibit multiple negative CIE pulses. An Earth system model of intermediate complexity with realistic

continental configuration and ocean bathymetry for the latest Permian conditions was used to simulate the carbon emission history using carbon isotope inversion of the $\delta^{13}C_{algae}$ records. Our best-fit model $\delta^{13}C_{source}$ value is determined be close to −15‰ by minimizing the root mean square error between modeled pH and boron isotope pH proxy estimates and between modeled sea surface temperature and oxygen isotope temperature proxy records. This suggests that atmospheric $pCO_2$ increases by 13× pre-extinction level with at least two separate pulses at a maximum rate of 4.5 Gt C $yr^{-1}$, each corresponding to the emplacement of the Siberian Traps volcanism, consistent with a largely volcanic source (53 to 77%) with smaller contributions from coal combustion or thermogenic methane during sill intrusion. Our work also highlights the air–sea disequilibrium evidenced by the significantly amplified CIE of the atmosphere, which supports our major conclusion of a rapid and massive $CO_2$ emission. Temperature-dependent silicate weathering feedback and organic carbon burial is insufficient to drive the full carbon isotope recovery to the pre-extinction level, with atmospheric $pCO_2$ remains at >3× larger than pre-event level, leading to the long-term Early Triassic warmth. Taken together, we suggest that it is the rapid and massive amount of largely volcanic $CO_2$ emission and associated feedbacks that led to the catastrophic mass extinction. It should be noted that despite the new astrochronology-based, compound-specific carbon isotope records and the advanced Earth system modeling results in the present study, there are still some unresolved questions that need to be addressed in future studies. Foremost, we would like to mention here 1) the chronology of the individual volcanic pulses and their exact correlation with the $\delta^{13}C$ shifts in the sedimentary records, 2) the links between the evolution of $\delta^{13}C_{source}$ and pulsed $CO_2$ degassing history, which is dependent on host-rock properties, and 3) that caution is warranted when interpreting the structure of carbon isotope records from a single site due to low density of data. Hence, future modeling efforts need a denser collection of globally representative ocean and atmosphere carbon isotope data with an astronomically tuned age model to produce an even more reliable inversion and to compare with the current results.

## Materials and Methods

**Material.** Details on the lithology and stratigraphy can be found in *SI Appendix* and ref. 49. In short, samples were collected from two parallel cores from three different units: an Upper Permian siltstone unit, the top of a Late Permian wackestone/grainstone unit existing of pebbly shale and in some places phosphorite, and a Lower Triassic siltstone/shale unit. A total of 19 samples were selected for lipid extraction from core 7128/12-U-01, and three samples were added from core 7129/10-U-01. Samples were taken from dark, organic rich shale/siltstone intervals, and one sample was taken from a condensed phosphorite bed (7129/10-U-01, 66.5 m). The two cores are correlated with each other based on the lithology by Bugge et al. (49)

**Bulk Organic Properties.** Analyses of total organic carbon and total organic C-isotopes were performed at ISO-analytical (http://www.iso-analytical.co.uk). Samples were treated with HCl before analyses in order to remove carbonates. Replicate analyses on standards show SDs of <0.5‰.

**Extraction, Isolation, and Analysis of *n*-alkanes.** Between 5 and 30 g of dry sediment of each sample was extracted with a mixture of DCM/MeOH (7.5/1 vol/vol) using a Soxhlet device. Solvents containing the *n*-alkanes were then evaporated using rotary evaporation. The total lipid extracts were separated using small columns with activated aluminum-oxide. An aliphatic hydrocarbon fraction was eluted with hexane, a polar fraction with a mixture of DCM:MeOH (1:1 vol/vol). The hydrocarbon fraction was further cleaned using urea adduction, after which the adduct fraction (containing straight chain hydrocarbons) was dissolved in hexane for further analyses. Adduct fractions were injected on gas chromatography to test yield and to check for contamination. Mass spectrometry was used to identify compounds, and isotope ratio mass spectrometry was used for carbon isotope analyses at Utrecht University. For more details on the chromatography methods and alkane indices, refer to *SI Appendix*.

**Palynology.** Following standard palynological methods palynomorphs were extracted from powdered rock-samples using hydrochloric acid and hydrofluoric acid and sieving over a 7-μm mesh at University of Oslo. Only major groups of palynomorphs were distinguished, which were then grouped together into major vegetation types.

**Time Series Analysis.** Cyclostratigraphy of total gamma ray intensity at site 7128/12-U-01 (49) provides a floating astrochronology for the carbon isotope records. Time series analysis for the construction of an astronomical time scale follows typical procedures described in (102). The analysis was performed using a software *Acycle* version 2.2 (102) described fully in *SI Appendix*.

**Earth System Model Experiments.** In order to provide insight on the most plausible $^{13}C$-depleted carbon sources that disrupted the global carbon cycle and during the EPME, we use isotope inversion in cGENIE with our collected compound specific carbon isotope data. cGENIE was set up to the Late Permian boundary conditions (such as paleogeography and paleobathymetry; *SI Appendix*). This model has a one-dimensional atmosphere and a three-dimensional ocean with 16 vertical layers. cGENIE considers the following geochemical tracers in the atmosphere and oceans via ATCHEM and BIOGEM modules: $O_2$, $CO_2$, DIC, alkalinity, carbonate ion, stable carbon isotopes ($^{12}C$ and $^{13}C$), and nutrients (nitrate and phosphate).

Over >100,000-y timescales, inputs of carbon from silicate weathering on land and volcanic outgassing balance the carbonate burial output (103). Over shorter timescales (i.e., millennial to tens of thousands of years), exogenic carbon sources, such as methane hydrate and organic matter oxidation, can lead to imbalances in the carbon cycle, driving rapid changes in atmospheric $pCO_2$. The biogeochemical model parameters and the rock weathering parameters are summarized in *SI Appendix*, Tables S1 and S2. The cGENIE model was run for 20,000 y in a closed system and another 200,000 y in an open system to allow for the balance between inputs from silicate weathering and degassing and outputs from carbonate burial. Afterward, seven experiments were set up using a range of plausible carbon sources ($\delta^{13}C_{source}$ = −9, −15, −18, −25, and −30‰ that cover the range of $\delta^{13}C$ values reported for $CO_2$ from Koolau melt inclusions in ref. 69; we also include $\delta^{13}C_{source}$ = −45‰ and −60‰ to cover scenarios associated with thermogenic and biogenic methane (104, 105) using the $\delta^{13}C_{algae}$ records to derive surface ocean $\delta^{13}C_{DIC}$ in the model inversion (refer to Fig. 5*F* for the evolution of surface ocean $\delta^{13}C_{DIC}$ records and *SI Appendix* for the associated assumptions). The initial $pCO_2$ was assumed to be ∼440 ppm based on stomatal ratio proxy using well-preserved cuticles from Southwest China (67), and the cGENIE model was tuned to an ice-free condition by adjusting the albedo. The models were run for 168,600 y to cover 251.941 to 251.772 Mya for short-chain, n-alkane–based inversion (from the onset of the CIE to 168.6 Kyr after the CIE onset; age 251.939 ± 0.031 Mya is marked in Fig. 5 as the age of the EPME based on ref. 106).

**Data Availability.** All data presented in this study are available in the supporting information. The code necessary to run the cGENIE model is available at https://github.com/derpycode/cgenie.muffin, and all model outputs and instructions to replicate the model results are accessible at https://zenodo.org/record/4543684.

**ACKNOWLEDGMENTS.** This work was funded by the Norwegian Research Council (Project 234005) to W.M.K., the US NSF (Grant 2026877) to Y.C., and National Natural Science Foundation of China (Grant 42072040) to M.L. We thank K. Nierop, D. Kasjaniuk, and A. van Leeuwen-Tolboom at Utrecht University and K. Backer Owe at the University of Oslo for technical support with the lab work. We also thank A. Mørk for help with sampling and L. Kump for discussions. Y.C. thanks A. Ridgwell for providing access to the University of California, Riverside domino cluster and Y. Wu for setting up the spin-ups. We are grateful to three anonymous reviewers, whose suggestions greatly improved the quality of the manuscript. Core material is stored and provided by SINTEF Petroleum Research in Trondheim.

1. S. D. Burgess, S. Bowring, S. Z. Shen, High-precision timeline for Earth's most severe extinction. *Proc. Natl. Acad. Sci. U.S.A.* **111**, 3316–3321 (2014).
2. S. Z. Shen *et al.*, Calibrating the end-Permian mass extinction. *Science* **334**, 1367–1372 (2011).
3. V. Davydov, Tunguska coals, Siberian sills and the Permian-Triassic extinction. *Earth Sci. Rev.* **212**, 103438 (2021).
4. S. D. Burgess, J. D. Muirhead, S. A. Bowring, Initial pulse of Siberian Traps sills as the trigger of the end-Permian mass extinction. *Nat. Commun.* **8**, 164 (2017).

5. S. D. Burgess, S. A. Bowring, High-precision geochronology confirms voluminous magmatism before, during, and after Earth's most severe extinction. *Sci. Adv.* **1**, e1500470 (2015).
6. B. A. Black, S. A. Gibson, Deep carbon and the life cycle of large igneous provinces. *Elements (Que)* **15**, 319–324 (2019).
7. B. A. Black *et al*., Systemic swings in end-Permian climate from Siberian Traps carbon and sulfur outgassing. *Nat. Geosci.* **11**, 949–954 (2018).
8. H. H. Svensen *et al*., Sills and gas generation in the Siberian Traps. *Philos. Trans.- Royal Soc., Math. Phys. Eng. Sci.* **376**, 20170080 (2018).
9. H. Svensen *et al*., Siberian gas venting and the end-Permian environmental crisis. *Earth Planet. Sci. Lett.* **277**, 490–500 (2009).
10. B. A. Black, M. Manga, Volatiles and the tempo of flood basalt magmatism. *Earth Planet. Sci. Lett.* **458**, 130–140 (2017).
11. M. Joachimski, A. Alekseev, A. Grigoryan, Y. A. Gatovsky, Siberian Trap volcanism, global warming and the Permian-Triassic mass extinction: New insights from Armenian Permian-Triassic sections. *Geol. Soc. Am. Bull.* **132**, 427–443 (2020).
12. M. M. Joachimski *et al*., Climate warming in the latest Permian and the Permian–Triassic mass extinction. *Geology* **40**, 195–198 (2012).
13. U. Brand *et al*., The end-Permian mass extinction: A rapid volcanic $CO_2$ and $CH_4$-climatic catastrophe. *Chem. Geol.* **322**, 121–144 (2012).
14. W.-q. Wang *et al*., A high-resolution middle to late Permian paleotemperature curve reconstructed using oxygen isotopes of well-preserved brachiopod shells. *Earth Planet. Sci. Lett.* **540**, 116245 (2020).
15. F. Zhang *et al*., Congruent Permian-Triassic δ238U records at Panthalassic and Tethyan sites: Confirmation of global-oceanic anoxia and validation of the U-isotope paleoredox proxy. *Geology* **46**, 327–330 (2018).
16. K. V. Lau *et al*., Marine anoxia and delayed Earth system recovery after the end-Permian extinction. *Proc. Natl. Acad. Sci. U.S.A.* **113**, 2360–2365 (2016).
17. H. Jurikova *et al*., Permian–Triassic mass extinction pulses driven by major marine carbon cycle perturbations. *Nat. Geosci.* **13**, 745–750 (2020).
18. J. L. Hinojosa *et al*., Evidence for end-Permian ocean acidification from calcium isotopes in biogenic apatite. *Geology* **40**, 743–746 (2012).
19. J. L. Payne *et al*., Calcium isotope constraints on the end-Permian mass extinction. *Proc. Natl. Acad. Sci. U.S.A.* **107**, 8543–8548 (2010).
20. M. O. Clarkson *et al*., Ocean acidification and the Permo-Triassic mass extinction. *Science* **348**, 229–232 (2015).
21. M. A. Sephton, D. Jiao, M. H. Engel, C. V. Looy, H. Visscher, Terrestrial acidification during the end-Permian biosphere crisis? *Geology* **43**, 159–162 (2015).
22. M. J. Benton, Hyperthermal-driven mass extinctions: Killing models during the Permian-Triassic mass extinction. *Philos. Trans.- Royal Soc., Math. Phys. Eng. Sci.* **376**, 20170076 (2018).
23. Y. Cui, L. R. Kump, Global warming and the end-Permian extinction event: Proxy and modeling perspectives. *Earth Sci. Rev.* **149**, 5–22 (2015).
24. Y. Wu *et al*., Six-fold increase of atmospheric $pCO_2$ during the Permian-Triassic mass extinction. *Nat. Commun.* **12**, 2137 (2021).
25. P. A. Hochuli, E. Hermann, J. O. Vigran, H. Bucher, H. Weissert, Rapid demise and recovery of plant ecosystems across the end-Permian extinction event. *Global Planet. Change* **74**, 144–155 (2010).
26. G. Eglinton, R. J. Hamilton, Leaf epicuticular waxes. *Science* **156**, 1322–1335 (1967).
27. J. Han, E. D. McCarthy, W. V. Hoeven, M. Calvin, W. H. Bradley, Organic geochemical studies, II. A preliminary report on the distribution of aliphatic hydrocarbons in algae, in bacteria, and in a recent lake sediment. *Proc. Natl. Acad. Sci. U.S.A.* **59**, 29–33 (1968).
28. J. Han, M. Calvin, Hydrocarbon distribution of algae and bacteria, and microbiological activity in sediments. *Proc. Natl. Acad. Sci. U.S.A.* **64**, 436–443 (1969).
29. M. A. Sephton *et al*., "Synchronous record of d13C shifts in the oceans and atmosphere at the end of the Permian" in *Catastrophic Events and Mass Extinctions: Impacts and Beyond*, C. Koeberl, K. G. MacLeod, Eds. (Geological Society of America Special Paper 356, Boulder, CO, 2002), pp. 455–462.
30. B. Nabbefeld *et al*., An integrated biomarker, isotopic and palaeoenvironmental study through the Late Permian event at Lusitaniadalen, Spitsbergen. *Earth Planet. Sci. Lett.* **291**, 84–96 (2010).
31. D. Batten, "Palynofacies and petroleum potential" in *Palynology: Principles and Applications*, J. Jansonius, D. C. McGregor, Eds. (American Association of Stratigraphic Palynologists' Foundation, Dallas, 1996), vol. 3, pp. 1065–1084.
32. Y. Cui, L. R. Kump, A. Ridgwell, Initial assessment on the carbon emission rate and climatic consequences during the end-Permian mass extinction. *Palaeogeogr. Palaeoclimatol. Palaeoecol.* **387**, 176–184 (2013).
33. J. L. Payne, M. E. Clapham, End-Permian mass extinction in the oceans: An ancient analog for the twenty-first century. *Annu. Rev. Earth Planet. Sci.* **40**, 89–111 (2012).
34. K. H. Freeman, R. D. Pancost, "Biomarkers for terrestrial plants and climate" in *Treatise on Geochemistry*, P. Falkowski, K. Freeman, Eds. (Elsevier, Amsterdam, 2014), vol. 12, pp. 395–416.
35. G. Mangerud, Palynostratigraphy of the Permian and lowermost Triassic succession, Finnmark Platform, Barents Sea. *Rev. Palaeobot. Palynol.* **82**, 317–349 (1994).
36. Y. Wu *et al*., Organic carbon isotopes in terrestrial Permian-Triassic boundary sections of North China: Implications for global carbon cycle perturbations. *Geol. Soc. Am. Bull.* **132**, 1106–1118 (2020).
37. G. J. Retallack, A. H. Jahren, Methane release from igneous intrusion of coal during Late Permian extinction events. *J. Geol.* **116**, 1–20 (2008).
38. B. A. Schubert, A. H. Jahren, The effect of atmospheric $CO_2$ concentration on carbon isotope fractionation in C3 land plants. *Geochim. Cosmochim. Acta* **96**, 29–43 (2012).
39. A. F. Diefendorf, K. E. Mueller, S. L. Wing, P. L. Koch, K. H. Freeman, Global patterns in leaf $^{13}C$ discrimination and implications for studies of past and future climate. *Proc. Natl. Acad. Sci. U.S.A.* **107**, 5738–5743 (2010).
40. H. Song, P. B. Wignall, J. Tong, H. Yin, Two pulses of extinction during the Permian-Triassic crisis. *Nat. Geosci.* **6**, 52–56 (2013).
41. A. Riccardi, L. R. Kump, M. A. Arthur, S. D'Hondt, Carbon isotopic evidence for chemocline upward excursions during the end-Permian event. *Palaeogeogr. Palaeoclimatol. Palaeoecol.* **248**, 73–81 (2007).
42. B. M. Thomas *et al*., Unique marine Permian-Triassic boundary section from Western Australia. *Aust. J. Earth Sci.* **51**, 423–430 (2004).
43. P. B. Wignall, A. Hallam, Anoxia as a cause of the Permian/Triassic extinction: Facies evidence from northern Italy and the western United States. *Palaeogeogr. Palaeoclimatol. Palaeoecol.* **93**, 21–46 (1992).
44. P. B. Wignall, R. J. Twitchett, Ocean anoxia and the end Permian mass extinction. *Science* **272**, 1155–1158 (1996).
45. Y. Isozaki, Permo-Triassic boundary superanoxia and stratified superocean: Records from lost deep sea. *Science* **276**, 235–238 (1997).
46. A. M. Dustira *et al*., Gradual onset of anoxia across the Permian-Triassic Boundary in Svalbard, Norway. *Palaeogeogr. Palaeoclimatol. Palaeoecol.* **374**, 303–313 (2013).
47. C. Mettam *et al*., "High-frequency fluctuations in redox conditions during the latest Permian mass extinction" in *Palaeogeography, Palaeoclimatology, Palaeoecology* (Elsevier, 2017), pp. 210–223.
48. S. E. Grasby *et al*., Progressive environmental deterioration in northwestern Pangea leading to the latest Permian extinction. *GSA Bulletin* **127**, 1331–1347 (2015).
49. T. Bugge *et al*., The Upper Palaeozoic succession on the Finnmark Platform, Barents Sea. *Nor. Geol. Tidsskr.* **75**, 3–30 (1995).
50. C. H. Eide, T. G. Klausen, D. Katkov, A. A. Suslova, W. Helland-Hansen, Linking an Early Triassic delta to antecedent topography: Source-to-sink study of the southwestern Barents Sea margin. *Geol. Soc. Am. Bull.* **130**, 263–283 (2018).
51. E. E. van Soelen, W. M. Kürschner, Late Permian to Early Triassic changes in acritarch assemblages and morphology in the Boreal Arctic: New data from the Finnmark Platform. *Palaeogeogr. Palaeoclimatol. Palaeoecol.* **505**, 120–127 (2018).
52. L. E. Hays, K. Grice, C. B. Foster, R. E. Summons, Biomarker and isotopic trends in a Permian–Triassic sedimentary section at Kap Stosch, Greenland. *Org. Geochem.* **43**, 67–82 (2012).
53. C. R. Witkowski, J. W. H. Weijers, B. Blais, S. Schouten, J. S. Sinninghe Damsté, Molecular fossils from phytoplankton reveal secular $Pco_2$ trend over the Phanerozoic. *Sci. Adv.* **4**, eaat4556 (2018).
54. M. Pagani, K. Freeman, N. Ohkouchi, K. Caldeira, Comparison of water column [CO2aq] with sedimentary alkenone-based estimates: A test of the alkenone-CO2 proxy. *Paleoceanography* **17**, 1069 (2002).
55. C. Korte, H. W. Kozur, Carbon-isotope stratigraphy across the Permian-Triassic boundary: A review. *J. Asian Earth Sci.* **39**, 215–235 (2010).
56. J. Payne, L. Kump, Evidence for recurrent Early Triassic massive volcanism from quantitative interpretation of carbon isotope fluctuations. *Earth Planet. Sci. Lett.* **256**, 264–277 (2007).
57. S. Kirtland Turner, P. M. Hull, L. R. Kump, A. Ridgwell, A probabilistic assessment of the rapidity of PETM onset. *Nat. Commun.* **8**, 353 (2017).
58. S. Z. Shen *et al*., End-Permian mass extinction pattern in the northern peri-Gondwanan region. *Palaeoworld* **15**, 3–30 (2006).
59. J. L. Payne *et al*., Large perturbations of the carbon cycle during recovery from the end-permian extinction. *Science* **305**, 506–509 (2004).
60. S. Richoz *et al*., Permian-Triassic boundary interval in the Middle East (Iran and N. Oman): Progressive environmental change from detailed carbonate carbon isotope marine curve and sedimentary evolution. *J. Asian Earth Sci.* **39**, 236–253 (2010).
61. M. Li *et al*., Astronomical tuning of the end-Permian extinction and the Early Triassic Epoch of South China and Germany. *Earth Planet. Sci. Lett.* **441**, 10–25 (2016).
62. H. Wu *et al*., Time-calibrated Milankovitch cycles for the late Permian. *Nat. Commun.* **4**, 2452 (2013).
63. Y. Cui, L. Kump, A. Ridgwell, "Spatial and temporal patterns of ocean acidification during the end-Permian mass extinction - An Earth system model evaluation" in *Volcanism and Global Environmental Change*, A. Schmidt, K. E. Fristad, L. T. Elkins-Tanton, Eds. (Cambridge University Press, Cambridge, United Kingdom, 2015), chap. 19, pp. 291–306.
64. M. Joachimski, A. Alekseev, A. Grigoryan, Y. A. Gatovsky, Siberian Trap volcanism, global warming and the Permian-Triassic mass extinction: New insights from Armenian Permian-Triassic sections. *Geol. Soc. Am. Bull.* **132**, 427–443 (2020).
65. B. Chen *et al*., Permian ice volume and palaeoclimate history: Oxygen isotope proxies revisited. *Gondwana Res.* **24**, 77–89 (2013).
66. M. Schobben *et al*., Discerning primary versus diagenetic signals in carbonate carbon and oxygen isotope records: An example from the Permian–Triassic boundary of Iran. *Chem. Geol.* **422**, 94–107 (2016).
67. H. Li, J. Yu, J. C. McElwain, C. Yiotis, Z.-Q. Chen, Reconstruction of atmospheric CO2 concentration during the late Changhsingian based on fossil conifers from the Dalong Formation in South China. *Palaeogeogr. Palaeoclimatol. Palaeoecol.* **519**, 37–48 (2019).
68. M. Javoy, F. Pineau, H. Delorme, Carbon and nitrogen isotopes in the mantle. *Chem. Geol.* **57**, 41–62 (1986).
69. E. Hauri, SIMS analysis of volatiles in silicate glasses, 2: Isotopes and abundances in Hawaiian melt inclusions. *Chem. Geol.* **183**, 115–141 (2002).
70. L. Elkins-Tanton *et al*., Field evidence for coal combustion links the 252 Ma Siberian Traps with global carbon disruption. *Geology* **48**, 986–991 (2020).
71. G. Peters *et al*., Carbon dioxide emissions continue to grow amidst slowly emerging climate policies. *Nat. Clim. Chang.* **10**, 3–6 (2020).
72. P. Friedlingstein *et al*., Global carbon budget 2019. *Earth Syst. Sci. Data* **11**, 1783–1838 (2019).
73. M. Gutjahr *et al*., Very large release of mostly volcanic carbon during the Palaeocene-Eocene Thermal Maximum. *Nature* **548**, 573–577 (2017).

74. A. D. Saunders, Two LIPs and two Earth-system crises: The impact of the North Atlantic Igneous Province and the Siberian Traps on the Earth-surface carbon cycle. *Geol. Mag.* **153**, 201–222 (2016).
75. Y. Cui *et al*., Slow release of fossil carbon during the Palaeocene-Eocene Thermal Maximum. *Nat. Geosci.* **4**, 481–485 (2011).
76. R. E. Zeebe, A. Ridgwell, J. C. Zachos, Anthropogenic carbon release rate unprecedented during the past 66 million years. *Nat. Geosci.* **9**, 325–329 (2016).
77. S. V. Sobolev *et al*., Linking mantle plumes, large igneous provinces and environmental catastrophes. *Nature* **477**, 312–316 (2011).
78. D. H. Rothman *et al*., Methanogenic burst in the end-Permian carbon cycle. *Proc. Natl. Acad. Sci. U.S.A.* **111**, 5462–5467 (2014).
79. M. A. Sephton *et al*., Catastrophic soil erosion during the end-Permian biotic crisis. *Geology* **33**, 941–944 (2005).
80. F. Zhang *et al*., Two distinct episodes of marine anoxia during the Permian-Triassic crisis evidenced by uranium isotopes in marine dolostones. *Geochim. Cosmochim. Acta* **287**, 165–179 (2020).
81. K. M. Meyer, M. Yu, A. B. Jost, B. M. Kelley, J. L. Payne, $\delta^{13}$C evidence that high primary productivity delayed recovery from end-Permian mass extinction. *Earth Planet. Sci. Lett.* **302**, 378–384 (2011).
82. M. Schobben *et al*., A nutrient control on marine anoxia during the end-Permian mass extinction. *Nat. Geosci.* **13**, 640–646 (2020).
83. J. C. Walker, J. F. Kasting, Effects of fuel and forest conservation on future levels of atmospheric carbon dioxide. *Global Planet. Change* **97**, 151–189 (1992).
84. J. Gaillardet, B. Dupré, P. Louvat, C. Allegre, Global silicate weathering and $CO_2$ consumption rates deduced from the chemistry of large rivers. *Chem. Geol.* **159**, 3–30 (1999).
85. C. Dessert, B. Dupré, J. Gaillardet, L. M. François, C. J. Allegre, Basalt weathering laws and the impact of basalt weathering on the global carbon cycle. *Chem. Geol.* **202**, 257–273 (2003).
86. A. J. West, A. Galy, M. Bickle, Tectonic and climatic controls on silicate weathering. *Earth Planet. Sci. Lett.* **235**, 211–228 (2005).
87. M. F. Schaller, J. D. Wright, D. V. Kent, P. E. Olsen, Rapid emplacement of the Central Atlantic Magmatic Province as a net sink for $CO_2$. *Earth Planet. Sci. Lett.* **323**, 27–39 (2012).
88. H. Sun *et al*., Rapid enhancement of chemical weathering recorded by extremely light seawater lithium isotopes at the Permian-Triassic boundary. *Proc. Natl. Acad. Sci. U.S.A.* **115**, 3782–3787 (2018).
89. R. Stallard, J. Edmond, Geochemistry of the Amazon: 2. The influence of geology and weathering environment on the dissolved load. *J. Geophys. Res. Oceans* **88**, 9671–9688 (1983).
90. L. R. Kump, Prolonged Late Permian-Early Triassic hyperthermal: Failure of climate regulation? *Philos. Trans. A. Math Phys. Eng. Sci.* **376**, 20170078 (2018).
91. J. Shen *et al*., Mercury evidence of intense volcanic effects on land during the Permian-Triassic transition. *Geology* **47**, 1117–1121 (2019).
92. D. Chu *et al*., Ecological disturbance in tropical peatlands prior to marine Permian-Triassic mass extinction. *Geology* **48**, 288–292 (2020).
93. S. E. Grasby, H. Sanei, B. Beauchamp, Catastrophic dispersion of coal fly ash into oceans during the latest Permian extinction. *Nat. Geosci.* **4**, 104–107 (2011).
94. S. E. Grasby *et al*., Isotopic signatures of mercury contamination in latest Permian oceans. *Geology* **45**, 55–58 (2017).
95. B. J. Burger, M. V. Estrada, M. S. Gustin, What caused Earth's largest mass extinction event? New evidence from the Permian-Triassic boundary in northeastern Utah. *Global Planet. Change* **177**, 81–100 (2019).
96. S. E. Grasby, X. Liu, R. Yin, R. E. Ernst, Z. Chen, Toxic mercury pulses into late Permian terrestrial and marine environments. *Geology* **48**, 830–833 (2020).
97. J. Dal Corso *et al*., Permo-Triassic boundary carbon and mercury cycling linked to terrestrial ecosystem collapse. *Nat. Commun.* **11**, 2962 (2020).
98. S. Ajayi *et al*., Evaluation of paleocene-eocene thermal maximum carbon isotope record completeness–An illustration of the potential of dynamic time warping in aligning paleo-proxy records. *Geochem., Geophys., Geosy.* **21**, e2019GC008620 (2020).
99. S. Kirtland Turner, A. Ridgwell, Development of a novel empirical framework for interpreting geological carbon isotope excursions, with implications for the rate of carbon injection across the PETM. *Earth Planet. Sci. Lett.* **435**, 1–13 (2016).
100. D. H. Rothman, Thresholds of catastrophe in the Earth system. *Sci. Adv.* **3**, e1700906 (2017).
101. D. H. Rothman, Characteristic disruptions of an excitable carbon cycle. *Proc. Natl. Acad. Sci. U.S.A.* **116**, 14813–14822 (2019).
102. M. Li, L. Hinnov, L. Kump, Acycle: Time-series analysis software for paleoclimate research and education. *Comput. Geosci.* **127**, 12–22 (2019).
103. G. Colbourn, A. Ridgwell, T. Lenton, The timescale of the silicate weathering negative feedback on atmospheric CO2. *Global Biogeochem. Cycles* **29**, 583–596 (2015).
104. J. Frieling *et al*., Extreme warmth and heat-stressed plankton in the tropics during the paleocene-eocene thermal maximum. *Sci. Adv.* **3**, e1600891 (2017).
105. J. Clayton, Geochemistry of coalbed gas–A review. *Int. J. Coal Geol.* **35**, 159–173 (1998).
106. S.-Z. Shen *et al*., A sudden end-Permian mass extinction in South China. *Geol. Soc. Am. Bull.* **131**, 205–223 (2018).
107. C. Korte, H. Kozur, Carbon isotope stratigraphy across the Permian/Triassic boundary at Jolfa (NW-Iran), Peitlerkofel (Sas de Pütia, Sass de Putia), Pufels (Bula, Bulla), Tesero (all three Southern Alps, Italy) and Gerennavár (BükkMts., Hungary). *J. Alp. Geol.* **47**, 119–135 (2005).
108. K. Zhang, X. Lai, J. Tong, H. Jiang, Progresses on study of conodont sequence for the GSSP section at Meishan, Changxing, Zhejiang Province, South China. *Acta Palaeontologica Sin.* **48**, 474–486 (2009).
109. H. W. Kozur, Biostratigraphy and event stratigraphy in Iran around the Permian-Triassic Boundary (PTB): Implications for the causes of the PTB biotic crisis. *Global Planet. Change* **55**, 155–176 (2007).
110. A. Ghaderi, L. Leda, M. Schobben, D. Korn, A. R. Ashouri, High-resolution stratigraphy of the Changhsingian (Late Permian) successions of NW Iran and the Transcaucasus based on lithological features, conodonts and ammonoids. *Foss. Rec. (Weinh.)* **17**, 41–57 (2014).
111. R. R. Bidigare *et al*., Consistent fractionation of 13C in nature and in the laboratory: Growth-rate effects in some haptophyte algae. *Global Biogeochem. Cycles* **11**, 279–292 (1997).
112. K. H. Freeman, J. M. Hayes, Fractionation of carbon isotopes by phytoplankton and estimates of ancient CO2 levels. *Global Biogeochem. Cycles* **6**, 185–198 (1992).
113. B. N. Popp, R. Takigiku, J. M. Hayes, J. W. Louda, E. W. Baker, The post-Paleozoic chronology and mechanism of $^{13}$C depletion in primary marine organic matter. *Am. J. Sci.* **289**, 436–454 (1989).